Inorganic Chemistry

Article

pubs.acs.org/IC

A New Partially Deprotonated Mixed-Valence Manganese(II,III) Hydroxide–Arsenate with Electronic Conductivity: Magnetic Properties of High- and Room-Temperature Sarkinite

Imanol de Pedro,[†,‡] Jose M. Rojo,[†] Jordi Rius,[§] Oriol Vallcorba,[§] Idoia Ruiz de Larramendi,[†] Jesús Rodríguez Fernández,[‡] Luis Lezama,[†] and Teofilo Rojo*[,†]

[†]Departamento de Química Inorgánica, Facultad de Ciencia y Tecnología, Universidad del País Vasco UPV/EHU, 48080 Bilbao, Spain

[‡]CITIMAC, Facultad de Ciencias, Universidad de Cantabria, 39005 Santander, Spain

[§]Institut de Ciència de Materials de Barcelona (CSIC), Campus de la UAB, 08193 Bellaterra, Catalunya, Spain

ABSTRACT: A new three-dimensional hydroxide–arsenate compound called compound **2** has been synthesized by heating (in air) of the sarkinite phase, $Mn_2(OH)AsO_4$ (compound **1**), with temperature and time control. The crystal structure of this high-temperature compound has been solved by Patterson-function direct methods. A relevant feature of this new material is that it is actually the first member of the adamite-type family with mixed-valence manganese(II,III) and electronic conductivity. Crystal data: a = 6.7367(5) Å, b = 7.5220(6) Å, c = 9.8117(6) Å, α = 92.410(4)°, β = 109.840(4)°, γ = 115.946(4)°, $P\bar{1}$. The unit cell content derived from Rietveld refinement is $Mn_8(O_4H_x)(AsO_4)_4$. Its framework, projected along [111], is characterized by rings of eight Mn atoms with the OH^-/O^{2-} inside the rings. These rings form an almost perfect hexagonal arrangement with the AsO_4 groups placed in between. Bond-valence analysis indicates both partial deprotonation ($x \cong 3$) and the presence of Mn in two different oxidation states (II and III), which is consistent with the electronic conductivity above 300 °C from electrochemical measurements. The electron paramagnetic resonance spectra of compound **1** and of its high-temperature form compound **2** show the presence of antiferromagnetic interactions with stronger magnetic coupling for the high-temperature phase. Magnetization measurements of room-temperature compound **1** show a complex magnetic behavior, with a three-dimensional antiferromagnetic ordering and magnetic anomalies at low temperatures, whereas for compound **2**, an ordered state is not reached. Magnetostructural correlations indicate that superexchange interactions via oxygen are present in both compounds. The values of the magnetic exchange pathways [Mn–O–Mn] are characteristic of antiferromagnetic couplings. Notwithstanding, the existence of competition between different magnetic interactions through superexchange pathways can cause the complex magnetic behavior of compound **1**. The loss of three-dimensional magnetic ordering by heating of compound **1** could well be based on the presence of Mn^{3+} ions (d^4) in compound **2**.

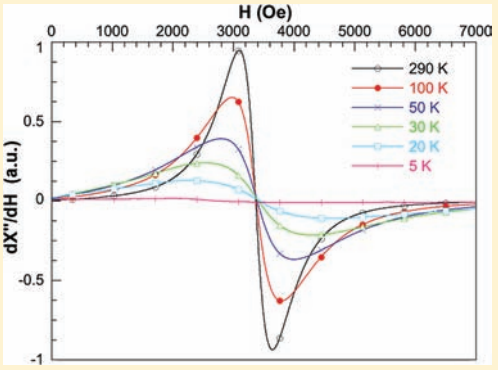

1. INTRODUCTION

Arsenate and phosphate minerals that contain mixed-valence cations, for example, $Ti^{3+}–Ti^{4+}$, $Mn^{2+}–Mn^{3+}$, $Fe^{2+}–Fe^{3+}$, etc., have interesting properties for ionic conductors, catalysts, and precursors for electrodes for Li-ion batteries in energy storage. In particular, langbeinite-type compounds, such as $NaTi_2(PO_4)_3$,[1] are used as superionic conductors,[2] iron hydroxylphosphate minerals like barbosalite $Fe_3(PO_4)_2(OH)_2$,[3] and rockbridgeite $Fe_5(PO4)_3(OH)_5$,[4] as efficient catalysts to produce methyl methacrylate, a very important intermediate in a large number of chemical processes,[5] or triplite[6] or adamite,[6] primary manganese–iron phosphates and arsenates, $M_2(F/OH)(XO_4)$ (M = Fe and Mn; X = P and As), and as precursors of electrode material like $LiFe(OH)PO_4$[7] and $LiFe(OH)AsO_4$[8] or $LiMnPO_4$[9] for rechargeable Li-ion batteries.

The complex structural chemistry of the adamite-type $[M_2(F/OH)(XO_4)]$ (where M = Zn, Mg, Co, Mn, Cu, etc.; X = P and As) family,[10−19] with a wide variety of polymorphs,[20,21] shows a large diversity of structural phases built up on $|MO_6|$ octahedra, $|MO_5|$ trigonal bipyramids linked to one another by |OH| ligands, and $|XO_4|$ [X = P and As] tetrahedra.[22−25] The structural and chemical richness of this family makes it particularly suitable for the study of the relationships between the physical properties and the crystal-packing features. Moreover, many of these compounds present interesting magnetic properties for insulation compounds, such as magnetic frustration, field-induced magnetic transitions,

Received: January 20, 2012
Published: April 20, 2012

   dx.doi.org/10.1021/ic3001569 | *Inorg. Chem.* 2012, 51, 5246–5256

incommensurate magnetic structures, etc.,[26−32] which have been analyzed with magnetostructural correlations.

Up to now, only two polymorphs of manganese hydroxide−arsenate, $Mn_2(OH)AsO_4$, are known, eveite[14] (space group *Pnnm*) and sarkinite[18] (space group *P*21/*c*). Their structures were reported many years ago, but the study of their physicochemical properties has been hampered because of the presence of impurities. So, our interest focused on finding the optimum conditions to synthesize these compounds with high purity. Recently, the sarkinite mineral was laboratory-synthesized as a pure phase under a mild hydrothermal reaction starting from the manganese arsenate octahydrate.[33] Taking into account the structural features of this mineral and the nature of the Mn ion ($S = {}^5/_2$), their magnetic properties are expected to be interesting. Moreover, the thermal behavior of this phase reveals a surprisingly large interval of stability from 300 to 650 °C,[33] not observed in the rest of the compounds of the adamite-type family. This thermal stability, using X-ray thermodiffractometry, was associated with a thermostructural change. The diffraction patterns showed, near to 300 °C, a rapid change of the crystallographic structure, stable up to 640 °C. A new adamite-type phase, compound **2**, is formed by heating (in air), which shows a transformation of color from white (compound **1**) to black (compound **2**) attributed to a change in the oxidation state of manganese Mn^{II}−Mn^{III} with a simultaneous loss of OH groups.[33]

In this paper, we report on the crystal structure of compound **2**, i.e., a new mixed-valence manganese(II,III) adamite-type compound $[M_2(O/OH)(XO_4)]$ showing electronic conductivity, as well as the magnetic properties of these phases.

2. EXPERIMENTAL SECTION

2.1. Synthesis and Preliminary Crystallographic Characterization. The synthesis of compound **1**, $Mn_2(OH)AsO_4$, using hydrothermal techniques was previously reported.[33] Room-temperature powder X-ray diffraction data of microcrystalline white samples were used to evaluate the purity of the product. The data were collected in the $10° \le 2\theta \le 90°$ range in steps of 0.02° with an integration time of 16 s per step using a Philips X'Pert-MPD X-ray diffractometer with secondary-beam graphite-monochromated Cu Kα radiation. The data were fitted using the pattern-matching (pm) routine of the program *FULLPROF*.[34] The resulting refined unit cell parameters are $a = 10.214(1)$ Å, $b = 13.603(1)$ Å, $c = 12.775(1)$ Å, $\beta = 108.87(1)°$, $V = 1679.72(1)$ Å^3, and $P2_1/a$, which are close to those reported from single-crystal data [$a = 10.210(1)$ Å, $b = 13.600(1)$ Å, $c = 12.771(2)$ Å, and $\beta = 108.74(1)°$].[18] Because no extra diffraction peaks were observed, it was concluded that the synthetic product (compound **1**) was pure and hence was used for studying its magnetic properties.

For the synthesis of compound **2**, about 1 g of compound **1** was transferred to an alumina boat and heated slowly under an air atmosphere flow as described in ref 33. The resultant powder was ground, cleaned, and dried over P_2O_5 for 24 h. The powder X-ray diffraction pattern of the high-temperature phase of sarkinite obtained at 500 °C was collected, at room temperature, on a Siemens D5000 diffractometer (Bragg−Brentano geometry, secondary graphite monochromator, and scintillation counter): measured 2θ interval 8−90°, Cu Kα_{12} radiation, 45 kV, 25 mA, step scan width 2θ 0.02°, step time 8 s, flat sample (to minimize the preferred orientation, the sample was side-loaded onto an aluminum sample holder). The pattern was indexed with *Treor84*[35] from 20 selected lines. The unit cell is triclinic $a = 6.735$ Å, $b = 7.523$ Å, $c = 10.142$ Å, $\alpha = 114.24°$, $\beta = 89.35°$, and $\gamma = 64.06°$. This cell was reduced and refined with the program *DAJUST2*[36] to $a = 6.7367(5)$ Å, $b = 7.5220(6)$ Å, $c = 9.8117(6)$ Å, $\alpha = 92.410(4)°$, $\beta = 109.840(4)°$, and $\gamma = 115.946(4)°$ with a zero-point shift equal to $-0.002(2)°$. Figures of merit of pm are $R_{wp(pm)} = 0.122$ and $\chi^2 = 1.29$. The extracted integrated intensities supplied by *DAJUST2* were used for structure determination.

2.2. Crystal Structure Solution of Compound 2. The crystal structure of compound **2** was solved by Patterson-function direct methods (*XLENS-PD6* code)[37] using intensity data up to a *d* spacing of 1.35 Å by assuming $P\bar{1}$ space group symmetry. The found Mn and As atomic positions were refined with the Rietveld *RIBOLS18* program.[38,39] The AsO_4 tetrahedra were refined as rigid bodies starting from random orientations (As−O distance is 1.68 Å). Once the AsO_4^{2-} anions oriented, the missing OH/O^{2-} were found from difference Fourier calculations and denoted by O3, O4, O5, and O6. The too short mutual distances and the fact that their individual occupancies refined to an average value of 0.56(2) indicated that O3, O4, O5, and O6 are disordered. From considerations of distance, these peaks could be split, unambiguously, into two sets of physically reasonable distributions. Final figures of merit are $R_{wp} = 12.98\%$ and $\chi^2 = 1.50$ (χ^2 of pm is 1.29). The refined atomic coordinates are listed in Table 1, and the corresponding Rietveld plot is reproduced in Figure 1. The unit cell content, derived from Rietveld refinement, is $Mn_8(O_4H_x)(AsO_4)_4$. Notice that the presence of Mn in a higher oxidation state than II forces *x* to be lower than 4 to preserve the charge balance. This point will be treated in section 3.

Table 1. Final Atomic Coordinates of Compound 2 Referring to Unit Cell $a = 6.7367$ Å, $b = 7.5220$ Å, $c = 9.8117$ Å, $\alpha = 92.410°$, $\beta = 109.840°$, and $\gamma = 115.946°$, with Standard Units in Parentheses ($B_{overall} = 3.5$ Å^2; Space Group $P\bar{1}$)

atom	*x*/*a*	*y*/*b*	*z*/*c*	occupancy
Mn1a	0.2167(16)	−0.1075(14)	0.5100(11)	1
Mn1b	0.1877(15)	0.3953(14)	0.0011(11)	1
Mn2a	−0.3178(17)	−0.0578(13)	0.1405(11)	1
Mn2b	0.3990(15)	0.4450(15)	0.6357(11)	1
As1	−0.2699(9)	−0.0386(8)	−0.1921(7)	1
As2	0.0281(11)	0.4576(8)	0.3068(7)	1
O1a	0.0291(59)	0.1087(53)	−0.1345(41)	1
O1b	−0.3325(59)	−0.2798(53)	−0.1863(41)	1
O1c	−0.3681(59)	0.0438(53)	−0.0801(41)	1
O1d	−0.4081(59)	−0.0272(53)	−0.3674(41)	1
O2a	−0.0815(59)	0.5932(53)	0.3661(41)	1
O2b	−0.1515(59)	0.2092(53)	0.2873(41)	1
O2c	0.3069(59)	0.5267(53)	0.4317(41)	1
O2d	0.0386(59)	0.5014(53)	0.1420(41)	1
O3	−0.4903(110)	−0.3387(99)	0.2043(76)	${}^1/_2$
O4	0.5299(118)	0.3882(97)	−0.0658(58)	${}^1/_2$
O5	−0.0507(104)	−0.0844(78)	−0.4659(73)	${}^1/_2$
O6	0.2980(103)	0.1910(84)	0.6561(61)	${}^1/_2$

For completion purposes, refinement in *P*1 was also carried out. This means almost doubling the number of refined parameters; however, the corresponding figures of merit ($R_{wp} = 12.61\%$; $\chi^2 = 1.47$) showed no significant improvement. Consequently, the atomic coordinates derived from the simpler $P\bar{1}$ refinement were preferred; i.e., coherently diffracting *P*1 domains, related by an inversion center, were assumed.

2.3. Physicochemical Characterization Techniques. The thermal behavior of Mn_2OHAsO_4 was previously reported using thermal analysis (TGA, DTA, and X-ray thermodiffractometry).[33] For the electrical property measurements, a pellet of compound **1** (0.96 cm diameter and 0.078 cm thickness) was used and coated with platinum meshes as an electrode. Electrochemical impedance spectroscopy (EIS) measurements were conducted using a Solartron 1260 impedance analyzer with a frequency range from 10^{-2} to 10^6 Hz. The effect of the temperature on the alternating-current (ac) characteristics was studied at equilibrium from room temperature to

dx.doi.org/10.1021/ic3001569 | Inorg. Chem. 2012, 51, 5246−5256

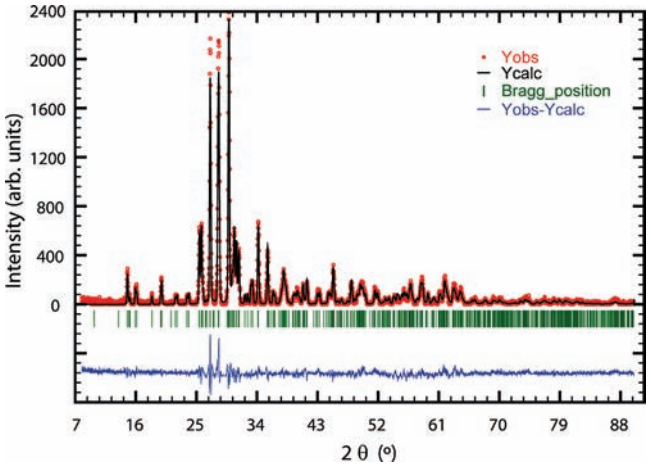

Figure 1. Observed (points) and calculated (line) powder diffraction patterns for compound **2** with a difference profile (bottom). The lines indicate the positions of the Bragg reflections.

500 °C, under zero direc-current (dc) current intensity and under air over a cycle of heating and cooling. Impedance diagrams were analyzed and fitted by the equivalent circuit method using *Zview* software. Resistance and capacitance values from the fitting of each semicircle in the EIS measurements were obtained by least-squares refinement. Spectroscopic measurements of both phases were studied by electron paramagnetic resonance (EPR). A Bruker ELEXSYS 500 spectrometer equipped with a superhigh-Q resonator ER-4123-SHQ, operating at X band, was used to record the EPR polycrystalline spectra. The magnetic field was calibrated by a NMR probe, and the frequency inside the cavity was determined with an integrated MW-frequency counter. The temperature was stabilized with an Oxford Instruments (ITC 4) regulator. Magnetic measurements of powdered samples were performed using a Quantum Design PPMS magnetometer; dc magnetic susceptibility curves were obtained while heating from 2 to 300 K in different applied magnetic fields, from 1 to 90 kOe, after cooling in either the presence (field cooling, FC) or absence (zero field cooling, ZFC) of the applied field; magnetization as a function of the field (H) was measured within $-85 \leq H/\text{kOe} \leq 85$ at 2 K after cooling of the sample in zero field; ac magnetic susceptibility measurements were performed with an alternate excitation field (H_{ac}) of 1 Oe and a frequency from 50 to 10000 Hz. The heat capacity was measured between 2 and 300 K in the same PPMS device with a standard relaxation method using a 2τ model. Compounds **1** and **2** were 8.96 and 7.45 mg plates obtained by compressing the original thin powder. In order to guarantee good thermal contact, apiezon N grease was used to glue the sample to the sample holder. The addenda (sample holder plus grease) was measured at different magnetic fields before sample measurements and then subtracted from the total heat capacity in order to get the sample heat capacity.

3. RESULTS AND DISCUSSION

3.1. Description of the Crystal Structure of compound 2. The framework structure of compound **1**, Mn_2OHAsO_4, is formed by three kinds of coordination polyhedra.[18] As atoms form quite regular AsO_4 tetrahedra while Mn atoms show two different coordination polyhedra: either distorted $MnO_4(OH)_2$ octahedra or distorted trigonal bipyramids, $MnO_4(OH)$. The O ligands of the AsO_4 tetrahedra are bonded to one As and two Mn atoms. The average Mn−O distance is 2.166 (16×), which corresponds to an average bond valence of 0.375 vu (valence units), so that the formal negative charge for each ligand is reached (1.25 + 2 × 0.375 = 2 vu). By heating of compound **1** in air, a phase transformation occurs at approximately 285 °C. The resulting compound **2** is stable up to 660 °C.[33] The present study indicates that the topologies of compounds **1** and **2** are similar, with the principal differences being concentrated in the OH^-/O^{2-} distribution and in the oxidation state of the Mn atoms. Figure 2 reproduces the four building units that,

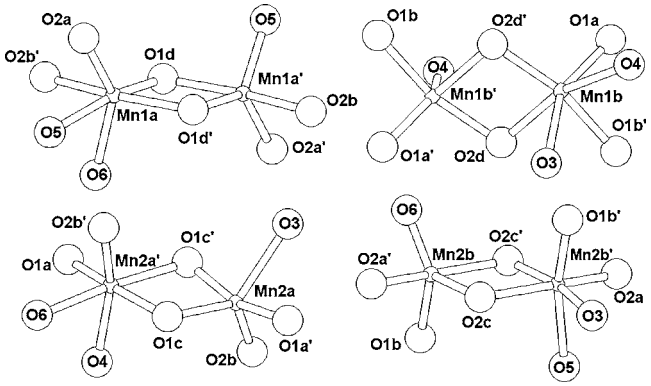

Figure 2. Building units of compound **2** with pseudoinversion centers relating Mn1a−Mn1a′, Mn1b−Mn1b′, Mn2a−Mn2a′, and Mn2b−Mn2b′ pairs at ($^1/_2$, 0, $^1/_2$), (0, $^1/_2$, 0), ($^1/_2$, 0, 0), and ($^1/_2$, $^1/_2$, $^1/_2$), respectively. Each building unit is formed by one distorted octahedron and one distorted trigonal bipyramid sharing one edge. These building units are bonded to the As atoms to give the high-temperature framework (O ligands have their labels outside the circle).

when bonded to the As atoms, span the framework of compound **2**. As for compound **1**, the coordination polyhedra of the Mn atoms in compound **2** are either distorted octahedra or trigonal bipyramids. The global mean Mn−O bond lengths of the octahedra and trigonal bipyramids depicted in Figure 2 are 2.20 and 2.12 Å, respectively, in good agreement with the values 2.21 and 2.13 given by Dal Negro et al. for compound **1**.[18] A perspective view of the unit cell along [111] is shown in Figure 3, where the alternate arrangement of octahedral and trigonal-bipyramidal Mn atoms can be seen.

The principal bond lengths and balance of bond valences for compound **2** are summarized in Table 2. The small standard deviation (0.06 vu) of the average of the bond-valence sums of

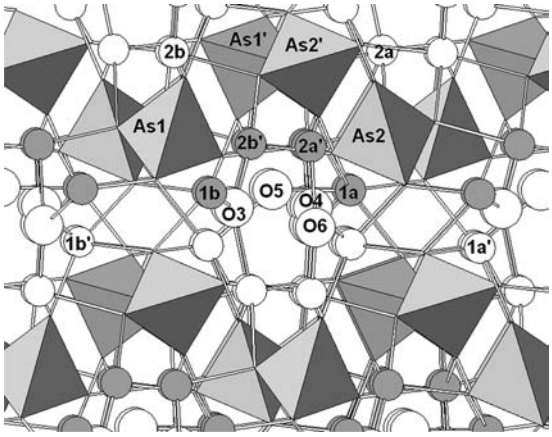

Figure 3. Unit cell of compound **2** viewed along [111] (*P*1 symmetry) clearly showing the Mn1a−Mn1a′, Mn1b−Mn1b′, Mn2a−Mn2a′, and Mn2b−Mn2b′ pairs related by pseudoinversion centers. Only O3, O4, O5, and O6 break the centrosymmetry. Small dark/empty circles represent octahedral/bipyramidal Mn atoms; large circles are O atoms not belonging to AsO_4 groups and present in the form of $(OH)^-$ or O^{2-}.

dx.doi.org/10.1021/ic3001569 | *Inorg. Chem.* 2012, 51, 5246−5256

Table 2. Balance of Bond Valences for Compound 2 Assuming Ideal AsO_4 Groups (As−O Distance: 1.68 Å)[a]

	As1, As2		Mn1a		Mn1b		Mn2a		Mn2b		
atom	*d*	*v*	*d*	*v*	*d*	*v*	*d*	*v*	*d*	*v*	$\sum v_{O(OH)}$
O1a	*1.68*	1.25			*2.08*	0.43	*2.16*	0.35			2.06[b]
O1b	*1.68*	1.25			*2.16*	0.35			*2.21*	0.31	1.94[b]
O1c	*1.68*	1.25					*2.29*	0.26			2.00[b]
							2.05	0.47			
O1d	*1.68*	1.25	*2.18*	0.34							1.93[b]
			2.20	0.32							
O2a	*1.68*	1.25	*2.22*	0.30					*2.02*	0.51	2.08[b]
O2b	*1.68*	1.25	*2.27*	0.27			*2.01*	0.52			2.06[b]
O2c	*1.68*	1.25							*2.09*	0.42	2.00[b]
									2.22	0.30	
O2d	*1.68*	1.25			*2.26*	0.28					1.92[b]
					2.14	0.37					
$\sum$		10		1.24[b]		1.45[b]		1.61[b]		1.56[b]	16
$^1/_2$ O3									*1.83*	0.82/2	0.69(3)[c]
					2.37	0.21/2	*2.16*	0.35/2			
$^1/_2$ O4					*2.62*	0.11/2					0.72(3)[c]
					1.75	1.00/2	*2.19*	0.33/2			
$^1/_2$ O5			*1.97*	0.57/2							0.52(3)[d]
			2.16	0.35/2					*2.65*	0.10/2	
$^1/_2$ O6			*2.35*	0.22/2					*1.77*	0.95/2	0.72(3)[c]
							2.26	0.28/2			
$\sum v_{As,Mn}$		10		1.82(6)		2.11(6)		2.09(6)		2.50(6)	18.64

[a] *d* = bond lengths in Å; *v* = bond valences in vu calculated for Mn−O with the expression $v = 10^{[1.75-d(v)]/0.91}$ (Allmann, 1975) ($\sigma \approx 0.041$ Å for As−O and Mn−O bond lengths; $\sigma \approx 0.07$ Å for Mn−OH ones). [b] After normalization by the factor 1.012 to reach the formal charge (16) of the eight O atoms of the two symmetry-unrelated AsO_4 groups. [c] The value for the $^1/_2[0.5(OH)^-, 0.5O^{2-}]$ composition is 0.75 vu. [d] The value for the $^1/_2(OH)^-$ composition is 0.50 vu.

the O atoms bonded to As confirms that the treatment of the AsO_4 groups as rigid bodies is, in the present case, a good approximation. From an inspection of Table 2, it follows that (i) the sum of the bond valences to $O^{2-}/(OH)^-$, 18.64 vu, is almost equal to the sum to As and Mn, i.e., 10 + 1.82 + 2.11 + 2.09 + 2.50 = 18.52 vu, (ii) the formal charges for pairs Mn1a−Mn1a′, Mn1b−Mn1b′, and Mn2a−Mn2a′ are close to 2+, and (iii) for the Mn2b−Mn2b′ pair, the formal charge is clearly around 2.5+.

The higher oxidation state of the Mn2b−Mn2b′ pair is in agreement with partial deprotonation during phase transformation, as suggested by de Pedro et al.[33] The amount of deprotonation can be estimated from the individual bond-valence sums at O3 (≈1.5 vu), O4 (≈1.5 vu), O5 (≈1.0 vu), and O6 (≈1.5 vu) because, according to the refined occupancies, no O vacancies are present. This means that the O5 hydroxyl group is always protonated and that the O3, O4, and O6 hydroxyl groups lose their proton in half of the cases. From the above considerations, the unit cell content of compound **2** must be close to $(Mn^{2+}_6, Mn^{2.5+}_2)$ $[(OH)_3O](AsO_4)_4$.

To allow for a direct comparison between compounds **1** and **2**, equally oriented portions of both crystal structures are shown in Figures 3 and 4, respectively. It is clear that both phases have very similar topologies and that the Mn atoms are also grouped, forming, in the projection, rings of eight members only differing in the arrangement of the hydroxyl groups. The bold lines in Figure 4 identify the five symmetrically independent pairs of Mn atoms that correspond to those of compound **2** in Figure 2. It is evident that the most relevant difference between both phases is that most pairs in compound **1** are formed by coordination polyhedra of the same type (only one has mixed types), whereas in compound **2**, all pairs are constituted by one octahedron and one trigonal bipyramid.

3.2. Impedance Spectroscopy. Typical electrochemical impedance spectra at different temperatures in the 10^{-2}−10^6 Hz frequency range are reported in the Nyquist plot (Figure 5).

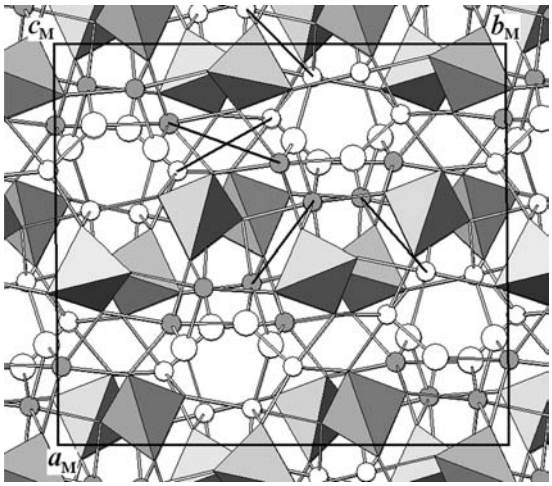

Figure 4. View of the unit cell of compound **1** along [001] showing, in the projection, four rings each of eight Mn atoms. The trigonal-bipyramidal and octahedral Mn atoms (dark and empty small circles, respectively) are alternately arranged up and down in the rings along *b*. This is in contrast with compound **2** (Figure 3), in which neighboring rings have the bipyramidal and octahedral Mn atoms equally oriented (inside each *P*1 domain). For the meaning of the bold lines connecting pairs of Mn atoms, see the text. Large circles represent hydroxyl groups.

dx.doi.org/10.1021/ic3001569 | Inorg. Chem. 2012, 51, 5246−5256

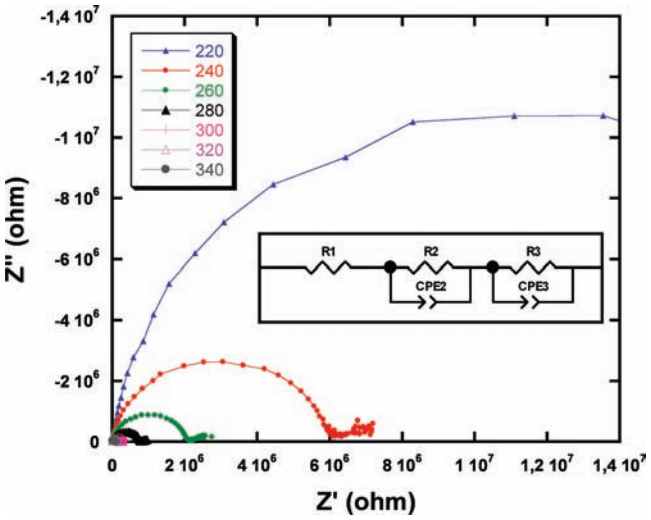

Figure 5. Impedance diagrams for compound **2**, under air, at different temperatures.

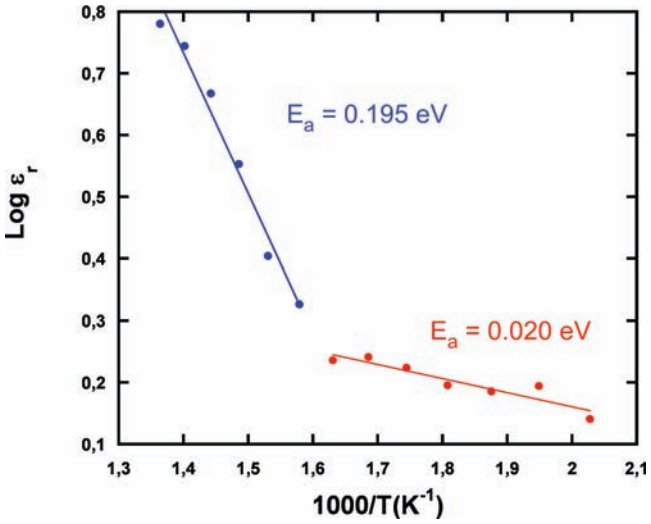

Figure 6. Variation of the dielectric constant with the temperature for compound **2**.

As expected, all of the semicircles became smaller upon an increase in the temperature and the difference of the intercepts of the asymmetric arc with the real axis decreased, indicating a lower resistance of the sample.

By using the *brickwork* model,[40] assuming that the sample is composed of cube-shaped grains separated from each other by a boundary, it is possible to separate three different contributions: the sample−electrode interface, grain boundary, and bulk regions. This model has been used for the fitting of the impedance data. The equivalent circuit that best fits the data is shown as an inset in this figure where R1, R2, and R3 are the ohmic resistance, diffusion in the grain (bulk), and grain boundary effects, respectively. R2 and R3 have constant phase elements in parallel to simulate the distribution of the relaxation time in the real system. Both semicircles are overlapped, preventing analysis of the results obtained for each process.

The complex dielectric constant is described by the equation $\varepsilon^* = \varepsilon' - j\varepsilon''$. The real part of the dielectric constant (ε') can be calculated by the following equation: $\varepsilon' = C(\omega)/C_0$. Taking into account the capacitance values obtained from the fit of the data, the study of the relative dielectric constant dependence of the temperature was carried out (see Figure 6).

Two behaviors showing different slopes are clearly distinguished. The first one is produced from room temperature to 340 °C and the second one above 360 °C, in good agreement with the results obtained from thermal analysis.[33] From the Arrhenius plot of the relative dielectric constant of the material, the activation energies of both behaviors were calculated as shown in Figure 6. This change in the dielectric constant at 350 °C is related to structural changes in the sample that produce a displacement or distortion in the accumulation of charge at interfaces.

Taking into account the phase transformation observed in the structural analysis, it is possible to assign the observed change in the dielectric constant to the oxidation of Mn, giving rise to the simultaneous existence in this compound of Mn cations in two different oxidation states, II+ and III+. This change in the oxidation state could produce the appearance of an electronic conductivity, probably of a hopping-type process. This phenomenon is produced at about 340 °C, while the phase transition is detected at 285 °C. This fact is due to the temperature difference between the sample and furnace during the electrochemical measurements. We have estimated a difference of about 40 °C at intermediate temperatures. In this way, the change in the dielectric behavior occurs at 300 °C, in good agreement with the results obtained from the crystal structure refinement. Finally, the maximum value obtained for the electronic conductivity in this material, 3.6417×10^{-6} S/cm at 460 °C, allows us to conclude that compound **2** presents a low conductivity level.

3.3. Magnetic Properties. *3.3.1. ESR Measurements.* The powder X-band EPR spectra of the title compounds at room temperature are given in Figure 7. In both cases, isotropic

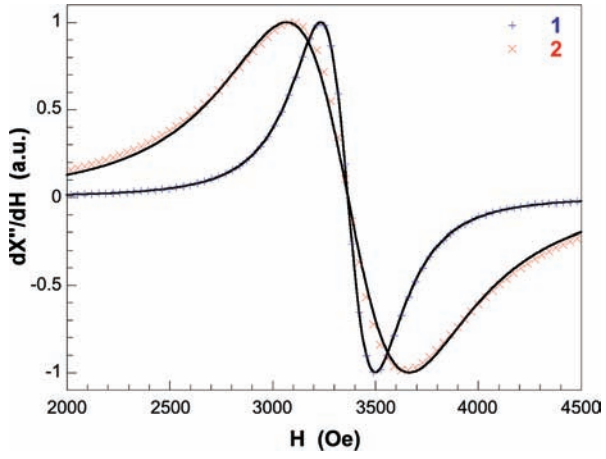

Figure 7. X-band EPR spectra of compounds **1** (1) and **2** (2) recorded at room temperature. Simulations of the experimental spectra to Lorentzian curves are represented by solid lines.

signals centered at about 3365 Oe were observed. The room-temperature $Mn_2(OH)AsO_4$ spectrum fits exactly to a Lorentzian curve with $g \approx 2.0$ and line width $\Delta H = 230$ Oe. The spectrum is characteristic of Mn^{II} ions in octahedral and trigonal-bipyramidal environments without large tetragonal distortion. In the case of compound **2**, although the Mn sites are similar to those observed in compound **1**, a broader signal with $g \approx 2.0$ and $\Delta H = 517$ Oe at room temperature was observed, with the best Lorentzian fit being appreciably worse.

dx.doi.org/10.1021/ic3001569 | *Inorg. Chem.* 2012, 51, 5246−5256

This result is probably due to the presence in the structure of Mn ions with different oxidation states, in good agreement with the existence of $MnO_4(OH)_2$–$MnO_4(OH)$ pairs with a formal charge close to 2.5+ deduced from the powder X-ray diffraction study.

The temperature dependences of the EPR spectra of compounds **1** and **2** between 4.2 and 290 K are shown in Figures 8 and 9. The *g* value for both phases remains apparently

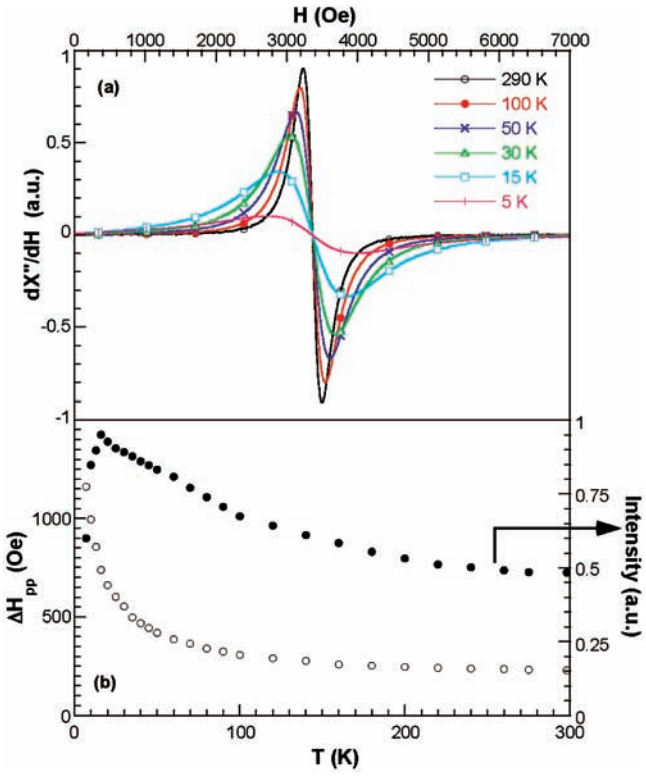

Figure 8. (a) Powder X-band EPR spectra at different temperatures and (b) temperature dependences of both the line width and intensity of the signal curves for compound **1**.

unchanged in all of the temperature ranges studied, and the amplitude of the signals decreases with a decrease in the temperature to 5 K for the room-temperature phase and approximately 20 K for compound **2**. At lower temperatures, the signals become practically undetectable (see Figures 8a and 9a). The temperature dependences of the intensity and line width of the signal, calculated by fitting of the experimental spectra to Lorentzian curves, are displayed in Figures 8b and 9b. As soon as the high-temperature condition ($kT \gg H_z$, H_{ex}, H_{disp}, ...) is satisfied, the line width is observed to have low temperature dependence. In fact, only a small increase is observed between room-temperature and 50 K probably because of the dipolar homogeneous broadening. Furthermore, when the temperature is decreased, the line width increases rapidly. This behavior is characteristic of systems with long-range spin correlation and, in this case, considering the thermal evolution of the intensity of the signal of both compounds **1** and **2**, the presence of antiferromagnetic interactions can be deduced.[41,42] Moreover, considering the higher temperature of the intensity maximum and the faster line width increases, stronger magnetic interactions are deduced for compound **2**.

The apparent temperature independence of the resonance field is also in good agreement with a three-dimensional

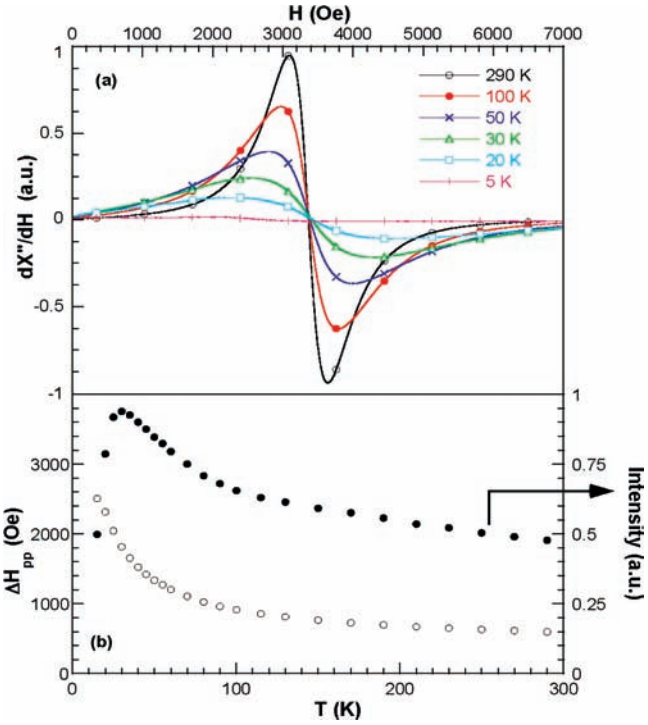

Figure 9. (a) Powder X-band EPR spectra at different temperatures and (b) temperature dependences of both the line width and intensity of the signal curves for compound **2**.

behavior with quasi-isotropic interactions. In any case, the presence of eight nonequivalent Mn^{II} sites in compound **1**, four five-coordinated and the other four six-coordinated, and the relatively large line widths observed imply that the conclusions obtained from the powder EPR spectra must be considered with caution. In fact, the observed isotropic signal is the result of the collapse by exchange of those expected for the eight different Mn^{II} ions.

3.3.2. Magnetization Measurements. dc Magnetic Susceptibility. Figure 10 shows the temperature dependence of the molar magnetic susceptibility (χ_m) and inverse susceptibility ($1/\chi_m$) curves of compounds **1** and **2**, measured at 1 kOe after cooling without an applied magnetic field (ZFC). At high temperature, $T \geq 150$ K, the thermal evolution of χ_m follows the classical Curie–Weiss law, with Weiss temperature θ_p = −114 and −125 K and Curie constant C_m = 3.25 and 2.98 emu·K/Mn-mol·Oe for compounds **1** and **2**, respectively. The negative θ_p value, together with the reduction of the effective magnetic moment ($\chi_m T$) observed when the temperature is decreasing (see upper insets of Figure 10), suggests a global antiferromagnetic behavior in both compounds. This behavior is in good agreement with the EPR data of both phases where the presence of antiferromagnetic interactions is observed, with it being stronger for compound **2** (higher θ_p value for compound **2**). The effective paramagnetic moment (μ_{eff}) values calculated for the paramagnetic region well above the Néel temperature because $\mu_{eff} = 2.828(C_m)^{1/2}$ gave the value of 5.1 and 4.88 μ_B/Mn ion, for compounds **1** and **2**, respectively. In the case of **1**, this value is near the theoretical one (μ_{eff} = 5.91 μ_B) obtained from $\mu_{eff} = g[S(S+1)]^{1/2}$, considering high-spin $S = {}^5/_2$ Mn cations with no orbital contribution, but shows a decrease in the case of **2** because of the presence of a small percentage of Mn^{III} ion (μ_{eff} = 4.90 μ_B). In addition, at low temperatures, the ZFC molar susceptibility (χ_m) at 1 kOe of

dx.doi.org/10.1021/ic3001569 | Inorg. Chem. 2012, 51, 5246–5256

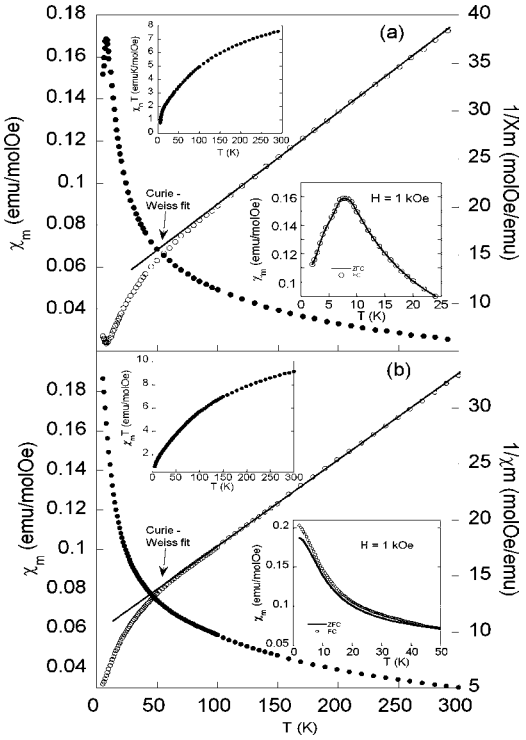

Figure 10. Temperature dependence of χ_m and $1/\chi_m$ for (a) compound **1** and (b) compound **2** measured under 1 kOe. The upper inset shows the temperature dependence of $\chi_m T$ and the lower inset an enlargement of the low-temperature region of ZFC−FC data. For reason of comparison, the χ_m values of compound **2** have been divided by 4.

compound **1** increases and reaches a rounded maximum at approximately 8 K, indicating the existence of three-dimensional long-range order (see the lower inset of Figure 10a). In contrast, compound **2** displays a continuous increase in the χ_m values from room temperature to 2 K (see the lower inset of Figure 10b), discarding the existence of long-range magnetic ordering.

The lower insets of Figure 10 show details of the low-temperature ZFC and FC molar susceptibility (χ_m) at 1 kOe of both compounds. On the one hand, the FC curve of compound **1** is reversible and follows the same pathway independently of how the temperature is approached, suggesting the absence of any ferromagnetic component. On the other hand, in compound **2**, the ZFC−FC curves show a small splitting characteristic of the presence of weak ferromagnetic interactions below 45 K. This behavior could be attributed to the presence of a small ferromagnetic impurity, Mn_3O_4 with a T_c of 42 K, as was observed in other phases.[44] The amount of this impurity, estimated from the ZFC−FC data, was lower than 0.5% by mass of Mn_3O_4, which was not detected by X-ray diffraction.

A more detailed study of the magnetic behavior of compound **1** has been carried out. The results are shown in Figure 11. The ZFC molar susceptibility (χ_m) measured under 1 kOe of compound **1** shows a broad peak with two characteristic temperatures (8 and 6.6 K) and a shoulder at around 3.9 K, marked by arrows, which could be associated with the existence of long-range magnetic ordering. Through the effect of the magnetic field, the shoulder is transformed into a new and well-defined maximum peak, located at 3.6, 3.1, and 2.3 K for applied magnetic fields of 20, 40, and 60 kOe,

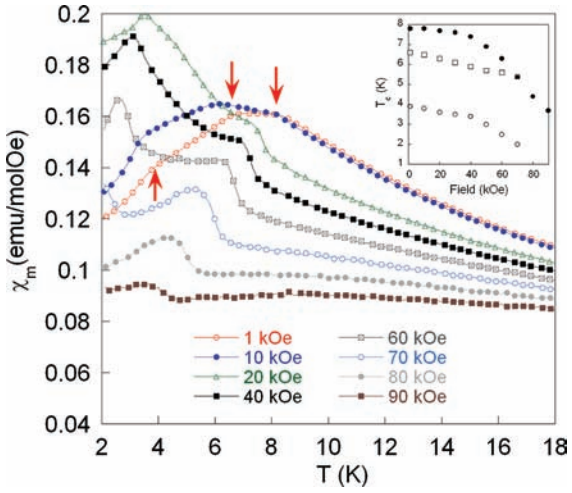

Figure 11. Low-temperature ZFC magnetic susceptibility of compound **1** at different fields from 1 to 90 kOe. The inset shows the temperature evolution of the critical temperatures with the applied magnetic field (see the text).

respectively, it disappearing or shifting below 2 K for higher magnetic fields (70 kOe). Furthermore, the broad peak evolves into a maximum peak (7.7 K) following to an inflection point (6.3 K) when the magnetic field is 20 kOe. The intensity of this peak subsequently decreases as the magnetic field increases, shifting to lower temperatures when the magnetic field rises. A plot of the field dependence of these critical temperatures is given in the inset of Figure 11. In this magnetic phase diagram, it can be observed that both critical temperatures (8 and 6.6 K) decrease as the magnetic field increases, with them collapsing at 70 kOe. These anomalies indicate a modification of the long-range spin arrangement with both the magnetic field and temperature, suggesting the existence of long-range antiferromagnetic ordering with a complex magnetic structure.

The field dependence on the magnetization with an applied magnetic field at 2 K of both compounds is represented in Figure 12. The $M(H)$ curve of compound **2** increases at low fields and tends toward saturation at higher fields. Its shape is

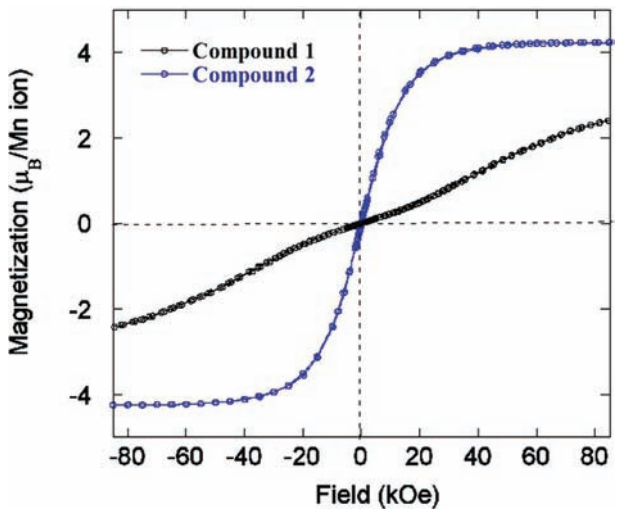

Figure 12. Magnetization versus applied magnetic field at 2 K for compounds **1** and **2**. The inset shows an enlargement of the low-magnetic-field region.

dx.doi.org/10.1021/ic3001569 | Inorg. Chem. 2012, 51, 5246−5256

quite similar to the Brillouin functions expected in paramagnetic materials with a magnetization value at 85 kOe of 4.28 μ_B/Mn ion. The magnetic moment obtained is close to that expected for the fully saturated free Mn^{II} ion value with the presence of a small percentage of Mn^{3+} ion (5 and 4.0 μ_B for Mn^{2+} and Mn^{3+} ions). However, for compound **1**, the magnetization changes in curvature at 20 kOe, probably because of the existence of a metamagnetic transition. Then, it continuously increases without showing any tendency to saturation up to 85 kOe. The magnetization value obtained at this magnetic field (2.48 μ_B/Mn ion) is much lower than that corresponding to the theoretical saturation, indicating the existence of a strong magnetocrystalline anisotropy.

ac Susceptibility. ac magnetic susceptibility measurements were performed with an alternate excitation field (H_{ac}) of amplitude 1 Oe and frequencies from 50 to 10000 Hz in order to study a possible dynamical magnetic behavior in the complex magnetic ordering of compound **1**; see Figure 13. In this figure,

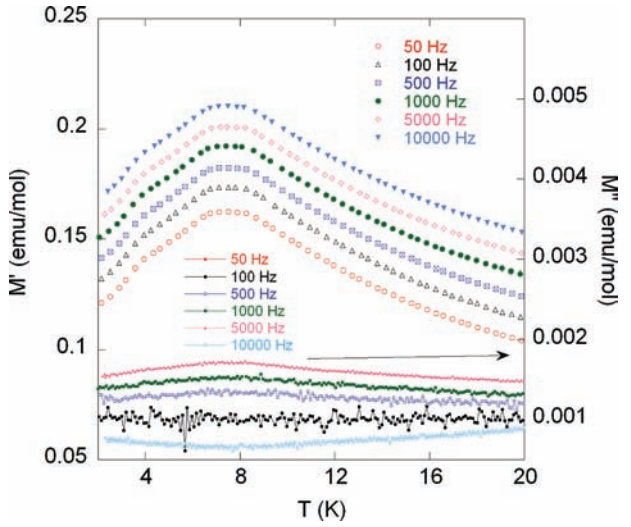

Figure 13. Temperature dependence of the real (χ') and imaginary (χ'') components of the ac magnetic susceptibility for compound **1** measured under an ac field h_{ac} = 1 Oe and at frequencies from 50 to 10000 Hz. The curves have been shifted 0.1 emu/mol·Oe for clarity.

the real and imaginary components of the susceptibility, χ' and χ'', are shifted upward and downward, respectively, with increasing frequency for clarity.

The dynamical susceptibility shows a broad peak in the real component of the susceptibility, χ', near 7.5 K and a shoulder close to 4 K, in good agreement with the dc magnetic susceptibility data. The lack of absorption in the out-of phase component, χ'', in this temperature region indicates the presence of a three-dimensional antiferromagnetic ordering,[45] in good agreement with the results obtained from dc magnetic susceptibility data. These magnetic anomalies are not frequency-dependent (over 3 decades of frequency) excluding the existence of spin glass transition or superparamagnetic blockage.[46,47] The ac susceptibility measurements carried out on compound **2** (not included) show an increase of χ' with decrease of the temperature, also in good agreement with the dc data.

Heat Capacity Measurements. The specific-heat measurements between 1.8 and 150 K in the absence of an external magnetic field are shown in Figure 14. Because of compound **2** having a unit cell nearly 4 times larger than that of compound

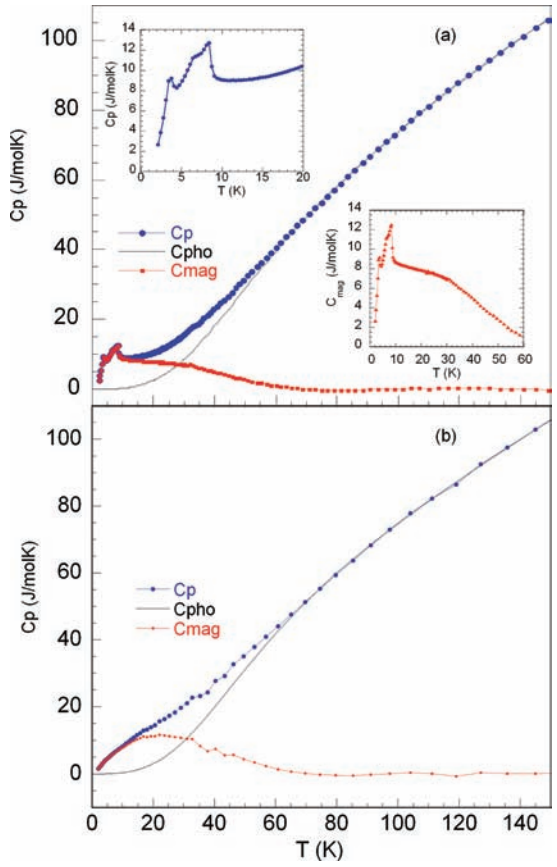

Figure 14. Specific heat of compounds **1** (a) and **2** (b) between 2 and 150 K. Experimental data (blue full dots), estimated phonon contribution (black full line), and magnetic contribution (red dots). For part a, the upper inset shows an enlargement of the low-temperature region and the lower inset the magnetic contribution below 60 K. Because compound **2** has a unit cell nearly 4 times larger than that of compound **1**, for reasons of comparison, in part b, we have divided all of the C_p values by 4.

1, its C_p values were divided by 4 for comparison. An enlargement around the magnetic transition has also been included for compound **1** (see the upper inset of Figure 14a). The curve shows two small peaks centered at 8.1 and 3.9 K and a shoulder around 6.6 K. These anomalies do not have the typical appearance of a simple second-order transition (λ shape) but could well be associated with the establishment of a complex three-dimensional antiferromagnetic ordering. Besides, the temperatures at which these anomalies appear are consistent with the magnetic anomalies observed in the molar magnetic susceptibility data (see Figure 11). For compound **2** (Figure 14b), the curve does not show magnetic peaks, discarding the existence of three-dimensional magnetic ordering.

The phonon heat capacity has been determined by fitting the high-temperature part of C_p (T > 80 K) to a Debye model[49] considering two different phonon spectra (heavy atoms, n_1, with a Debye temperature θ_1 and light atoms, n_2, with a Debye temperature θ_2), as was successfully used for other hydroxide compounds of the adamite-type family.[26,31] The best fit is depicted as a continuous line in Figure 14, with it being obtained with the following parameters: θ_1 = 260 and 267 K, θ_2 = 972 and 1001 K, and n_1 = 3.6 ions for **1** and **2**, respectively. The magnetic contribution to the heat capacity (C_{mag}) has been

dx.doi.org/10.1021/ic3001569 | Inorg. Chem. 2012, 51, 5246–5256

obtained by subtracting the corresponding phonon contribution (C_{pho}). In compound **1**, apart from the magnetic anomalies below 10 K, which are associated with the appearance of the antiferromagnetic three-dimensional magnetic ordering, a broad magnetic contribution still subsists at higher temperatures, as can be better observed in the lower inset of Figure 14a. For compound **2**, a broad magnetic contribution also appears below 60 K. One of the most plausible explanations for this magnetic anomaly is the contribution to the magnetic heat capacity of the Mn−Mn magnetic coupling in the form of two-dimensional or short-range magnetic ordering.[30] These would be located in the different polyhedra sharing of the complex magnetic structure of **1** and **2** that will be explained later from magnetostructural correlation data. The magnetic entropy, $S_m = \int(C_{mag}/T)\,dT$ (not shown) for both compounds, tends to saturate well above the magnetic transition, at around 80 K, with values of 26.35 and 23.30 J/mol·K for **1** and **2**, respectively. The magnetic entropy of compound **2** is close to the theoretical value $S_{mag} = 2R\ln(2S + 1)$, with $S = {}^5/_2$ for Mn^{2+} (29.68 J/mol·K), exhibiting a decrease in the case of compound **2** because of the presence of a small percentage of Mn^{III} ions.

The thermal evolution of the heat capacity measurements for compound **1** at different magnetic fields is shown in Figure 15.

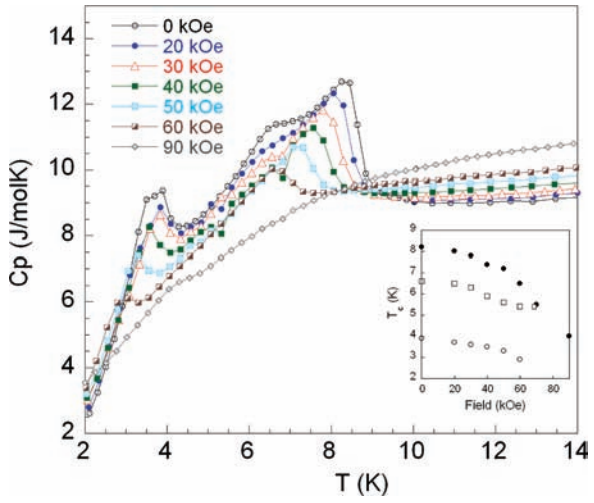

Figure 15. Specific heat as a function of the temperature in the presence of external magnetic fields ($H \leq 90$ kOe) of compound **1**. The lower inset shows the temperature evolution of magnetic anomalies with the applied magnetic field.

The curves reveal that the magnetic anomalies below 10 K, associated with the complex three-dimensional ordering, decrease in height and move toward lower temperatures as the applied field increases. This magnetic behavior is expected when antiferromagnetic transitions are present. The magnetic phase diagram obtained from C_p data is depicted in the inset of Figure 15. As can be seen, all critical temperatures decrease as the magnetic field increases, first slowly and then abruptly as the field approaches 90 kOe, in good agreement with the evolution observed in the susceptibility data.

3.3.3. Magnetostructural Correlations of Compounds 1 and 2. Knowledge of the crystal structures of compounds **1** and **2** enables presentation of the potential pathways of antiferromagnetic coupling between electrons of Mn ions. If we consider the structural features of these phases, we can deduce that direct Mn−Mn interactions are not present. The crystal structures of both phases show four manganese form $[MnO_4(OH)_2]$ distorted octahedra, while the remaining ones are linked to five anions to perform distorted trigonal bipyramids $[MnO_4(OH)]$. In the case of compound **1**, each octahedron shares three edges with nearby octahedra, except one Mn octahedron, which shares one edge with a trigonal bipyramid. In this way, it is possible to single out distortion chains built up by different polyhedra sharing (see Figure 16a).

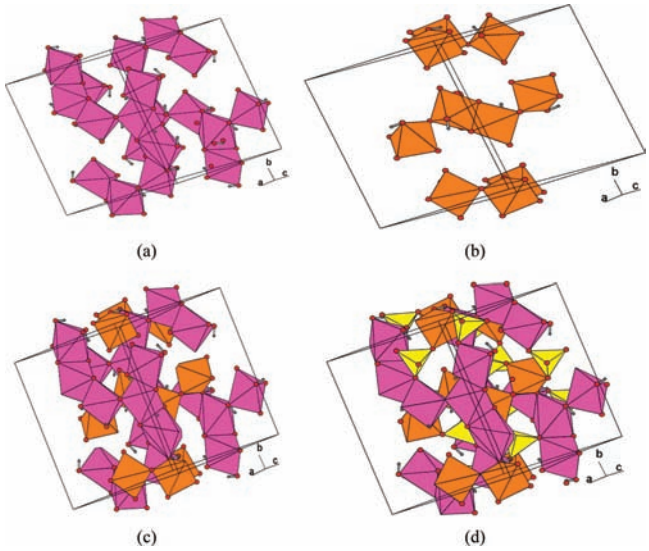

Figure 16. Different polyhedral sharing for compound **1**: (a) $[MnO_4(OH)_2]$ octahedra (blue); (b) trigonal bipyramids $[MnO_4(OH)]$ (red); (c) octahedral and trigonal-bipyramidal sharing; (d) linkage between octahedra and trigonal bipyramids propagated via $|AsO_4|$ tetrahedra (yellow).

Furthermore, with the exception of one Mn, each trigonal bipyramid shares one edge with a similar polyhedron, two vertices with two trigonal bipyramids (see Figure 16b), and the remaining vertex with two octahedra (see Figure 16c). The linkage between the trigonal bipyramids and the octahedra occurs through the vertex occupied by the hydroxyl groups with a mean exchange angle of 130°. In the edge-sharing $[Mn_2O_6(OH)_2]$ trigonal-bipyramidal and $[MnO_4(OH)_2]$ octahedral chains, the main superexchange intradimer interactions are located via oxygen involving metal d_{x2-y2} orbitals, whose angles range from 94.7° to 114.9°. For compound **2**, although the topology is very similar, all pairs are constituted by one octahedron and one trigonal bipyramid (see Figure 2) forming, in projection, rings of eight members (see Figure 3). In this way, magnetic couplings are presented via oxygen in the edge-sharing $[Mn_2O_7(OH)_2]$ pairs whose angles range from 100.1° to 108.3°. The superexchange interactions are well understood for a simple cation−anion−cation pathway with interactions that are strongly antiferromagnetic for a linear 180° metal−O−metal bond angle.[30,49] Considering the angles of the main superexchange interactions of these phases, compound **2** could show stronger antiferromagnetic coupling than compound **1**, in good agreement with the magnetic data. Finally, in both phases, the arsenic tetrahedral ensures a further crystal linkage between the different polyhedra (see Figures 3 and 16d). The magnetic interactions propagated via $|AsO_4|$ tetrahedra characterized by both the O−As−O and As−O−Mn angles could induce a three-dimensional antiferromagnetic ordering, as was observed

dx.doi.org/10.1021/ic3001569 | Inorg. Chem. 2012, 51, 5246−5256

in other cobalt adamite-type compounds $Co_2(OH)(XO_4)$ (X = P and As).[50] Taking into account that the partial substitution of Mn^{II} d^5 ($S = {}^5/_2$) by Mn^{III} d^4 ($S = 2$) by heating modifies the nature of some magnetic interactions in the framework, with the long-range magnetic ordering disappearing, it is reasonable to assume that some of these could disappear. However, this discussion must be considered with caution and high-resolution neutron powder diffraction data will be necessary for a better understanding of the complex magnetic structure of these phases.

4. CONCLUDING REMARKS

A new three-dimensional arsenate (compound **2**) of formula $Mn_8(O_4H_x)(AsO_4)_4$ with $x \cong 3$ has been synthesized by heating sarkinite in air at 500 °C. The close structural relationship between compounds **1** and **2** becomes apparent if the triclinic unit cell (a, b, c) of compound **2** is transformed into a body-centered one according to (a_B, b_B, c_B) = (a, b, c) (0, −1, 1/1, 0, 1/−1, 0, 1). The resulting centered unit cell with parameters a_B = 12.61, b_B = 6.74, c_B = 10.14 Å, α_B = 90.65, β_B = 107.98, and γ_B = 90.18° is very similar to the unit cell of compound **1** (with doubled b_B parameter); i.e., a_M = 12.78, b_M = 13.60, c_M = 10.21 Å, α_M = 90, β_M = 108.9, and γ_M = 90°. The diffraction pattern of compound **2** has been refined by assuming the existence of grains formed by coherently diffracting domains of $P1$ symmetry related by a symmetry center. As for compound **1**, the coordination polyhedra of the Mn atoms are either distorted octahedra or trigonal bipyramids. The global mean Mn−O bond lengths of the octahedra and trigonal bipyramids are 2.20 and 2.12 Å, respectively, in good agreement with the values 2.21 and 2.13 given by dal Negro et al.[18] for single-crystal data. The higher oxidation state of the Mn2b−Mn2b′ pair (around 2.5+) is in agreement with partial deprotonation during phase transformation, as suggested by de Pedro et al.[33] From the four symmetry-independent hydroxyl groups, only three are partially deprotonated, with all three showing the same approximate composition, i.e., $\approx {}^1/_2(OH) + {}^1/_2O$. This yields a unit cell content of $(Mn^{2+}{}_6, Mn^{2.5+}{}_2)[(OH)_3O](AsO_4)_4$. The simultaneous existence in this compound of Mn cations in two different oxidation states, II + and III+, produces the appearance of an electronic conductivity, probably of a hopping-type process, with a small conductivity level. EPR spectroscopy confirms the presence of both Mn^{2+} and Mn^{3+} ions on compound **2**, as well as the existence of a strong spin correlation below 30 K in this phase, despite the absence of three-dimensional magnetic ordering deduced from the magnetic susceptibility and heat capacity measurements. However, compound **1** shows the existence of a complex three-dimensional antiferromagnetic ordering below 10 K, strongly influenced by the magnetic field. Magnetic susceptibility and heat capacity data reveal three critical temperatures associated with the long-range antiferromagnetic ordering. The loss of magnetic ordering by heating of compound **1** could well be based on the presence of the Mn^{3+} ions in compound **2** (d^4). The different distributions of Mn^{3+} in each sublattice of polyhedra, $[[MnO_4(OH)_2]$ distorted octahedra and trigonal bipyramids $[MnO_4(OH)]$, decreases the magnetic couplings, with the three-dimensional ordering disappearing.

AUTHOR INFORMATION

Corresponding Author

*E-mail: teo.rojo@ehu.es.

Notes

The authors declare no competing financial interest.

ACKNOWLEDGMENTS

This work was financially supported by the Basque Country Government Grant IT-312-07 and by MEC research projects (MAT2011-27573-C04-01, MAT2010-19442, MAT2009-07967, and Consolider NANOSELECT CSD2007-00041), which we gratefully acknowledge.

REFERENCES

(1) Leclaire, A.; Benmoussa, A.; Borel, M. M.; Grandin, A.; Raveau, B. *J. Solid State Chem.* **1989**, *78*, 227.

(2) Carvajal, J. J.; Aznar, A.; Sole, R.; Gavalda, J.; Massons, J.; Solans, X.; Aguilo, M.; Diaz, F. *Chem. Mater.* **2003**, *15*, 204.

(3) (a) Redhammer, G. J.; Tippelt, G.; Roth, G.; Lottermoser, W.; Amthauer, G. *Phys. Chem. Miner.* **2000**, *27*, 419. (b) Schmid-Beurmann, P. *J. Solid State Chem.* **2000**, *153*, 237.

(4) (a) Moore, P. B. *Science* **1969**, *164*, 1063. (b) Schmid-Beurmann, P. *J. Mater. Chem.* **2001**, *11*, 660.

(5) Millet, J. M. M. *Catal. Rev. Sci. Eng.* **1998**, *40*, 1.

(6) Huminicki, D. M. C.; Hawthorne, F. C. *Rev. Mineral. Geochem.* **2002**, *48*, 28.

(7) Marx, N.; Croguennec, L.; Carlier, D.; Bourgeois, L.; Kubiak, P.; Le Cras, F.; Delmas, C. *Chem. Mater.* **2010**, *22*, 1854.

(8) Wiggin, S. B.; Hughes, R. W.; Price, D. J.; Weller, M. T. *Dalton Trans.* **2007**, 2935.

(9) Delacourt, C.; Poizot, P.; Morcrette, M.; Tarascon, J. M.; Masquelier, C. *Chem. Mater.* **2004**, *16*, 99.

(10) Moore, P. B.; Smyth, J. R. *Am. Mineral.* **1968**, *53*, 1841.

(11) Cordsen, A. *Am. Mineral.* **1978**, *16*, 153.

(12) Mills, S. J.; Kampf, A. R.; Poirier, G.; Raudsepp, M.; Steele, I. M. *Miner. Petrol.* **2010**, *99*, 113.

(13) Braithwaite, R. S. W.; Prichard, R. G.; Paar, W. H.; Pattrick, R. A. D. *Mineral. Mag.* **2005**, *69* (2), 145.

(14) Kolisch, U. *Acta Crystallogr., Sect. E* **2003**, *59* (9), 125.

(15) (a) Taasti, K. I.; Christensen, A. N.; Norby, P.; Hanson, J. C.; Lebech, B.; Jakobsen, A. H. J.; Skibsted, J. *J. Solid State Chem.* **2002**, *164*, 4250.

(16) Chukanov, N. V.; Yu Pushcharovsky, D.; Zubkova, N. V.; Pekov, I. V.; Pasero, M.; Merlino, S.; Möckel, S.; Rabadanov, M. Kh.; Belakovskiy, D. I. *Trans. (Dokl.) Russ. Acad. Sci./Earth Sci. Sect.* **2007**, *415A*, 841.

(17) Li, C.; Yang, H.; Downs, R. T. *Acta Crystallogr., Sect. A* **2008**, *E64*, i60.

(18) Dal Negro, A.; Guiseppetti, G.; Martin Pozas, J. M. *Tscherm. Mineral. Petrol. Mitt.* **1974**, *21*, 246.

(19) Williams, P. A.; Leverett, P.; Birch, W. D.; Hibbs, D. E.; Kolitsch, U.; Mihajlović, T. *J. Mineral.* **2006**, *12* (3), 7.

(20) Raade, G.; Mladeck, M. H. *Lithos.* **1979**, *12*, 283.

(21) Raade, G.; Rømming, C. *Z. Kristallogr.* **1986**, *177*, 1.

(22) Nord, A. G.; Kierkegaard, P.; Arber, G. *Chem. Commun.* **1988**, *6*, 1.

(23) Strunz, H.; Nickel, E. H. *Strunz Mineralogical Tables*; E. Scheweizebart'sche Verlagsbuchhandlung : Stuttgart, Germany, 2001.

(24) Anthony, J. W.; Bideaux, R. A.; Bladh, K. W.; Nichols, M. C. *Handbook of mineralogy: Arsenates, phosphates, vanadates*; Mineral Data Publishing: Tucson, AZ, 2000; Vol. *IV*.

(25) Kanazawa, T. *Inorganic Phosphate Materials*; Elsevier Science Publishers: Amsterdam, The Netherlands, 1989.

(26) Rojo, J. M.; Mesa, J. L.; Lezama, L.; Pizarro, J. L.; Arriortua, M. I.; Rodriguez Fernandez, J.; Barberis, G. E.; Rojo, T. *Phys. Rev. B* **2002**, *66*, 094406.

(27) De Pedro, I.; Rojo, J. M.; Jubera, V.; Rodrıíguez Fernández, J.; Sánchez Marcos, J.; Lezama, L.; Rojo, T. *J. Mater. Chem.* **2004**, *14*, 1157.
(28) de Pedro, I.; Rojo, J. M.; Pizarro, J. L.; Rodríguez Fernández, J.; Sánchez Marcos, J.; Fernández-Diaz, M. T.; Arriortua, M. I.; Rojo, T. *J. Phys.: Condens. Matter* **2006**, *18*, 3767.
(29) de Pedro, I.; Rojo, J. M.; Pizarro, J. L.; Rodríguez Fernández, J.; Sánchez Marcos, J.; Fernández-Diaz, M. T.; Arriortua, M. I.; Rojo, T. *J. Mater. Chem.* **2007**, *17*, 3915.
(30) de Pedro, I.; Rojo, J. M.; Rodríguez Fernández, J.; Lezama, L.; Rojo, T. *Eur. J. Inorg. Chem.* **2010**, 2514.
(31) de Pedro, I.; Rojo, J. M.; Rodríguez Fernández, J.; Fernández-Díaz, M. T.; Rojo, T. *Phys. Rev. B* **2010**, *81*, 134431.
(32) Kurmoo, M. *Chem. Soc. Rev.* **2009**, *38* (5), 1353.
(33) de Pedro, I.; Rojo, J. M.; Insausti, M.; Arriortua, M. I.; Rojo, T. *Z. Anorg. Allg. Chem.* **2005**, *631*, 2096.
(34) FULLPROF Program for Rietveld Refinement and Pattern Matching Analysis of Powder Patterns and later unpublished versions: Rodríguez-Carvajal, J. *Physica B* **1993**, *192*, 55. The program is a strongly modified version of that described by: Wiles, D. B.; Young, R. A. *J. Appl. Crystallogr.* **1981**, *14*, 149.
(35) Treor84—Trial & error program for indexing of unknown powder patterns: Werner, P. E. *Z. Kristallogr.* **1964**, *120*, 375.
(36) Rius, J.; Miravitlles, C.; Amigó, J. M.; Reventós, M. M.; Louër, D. *Anal. Quím. Int. Ed.* **1996**, *92*, 223. *DAJUST2* code available at WWW.icmab.es/xlens.
(37) Rius, J. *Acta Crystallogr.* **2011**, *A67*, 63. *XLENS_PD6* code available at www.icmab.es/xlens.
(38) Rius, J. *RIBOLS18—A computer program for least-squares refinement from powder diffraction data*; Institut de Ciència de Materials de Barcelona (CSIC): Barcelona, Spain, 2009.
(39) Allmann, R. *Monatsh. Chem.* **1975**, *106*, 779.
(40) Irvine, J. T. S.; Sinclair, D. C.; West, A. R. *Adv. Mater.* **1990**, *2*, 132−138.
(41) Bencini, A.; Gatteschi, D. *EPR of Exchange Coupled Systems*; Springer-Verlag: Berlin/Heidelberg, 1990.
(42) Hitzfeld, M.; Ziemann, P.; Buckel, W.; Claus, H. *Phys. Rev. B* **1984**, *29*, 5023.
(43) Seo, W. S.; Jo, H. H.; Lee, K.; Kim, B.; Oh, S. J.; Park, J. T. *Angew. Chem., Int. Ed.* **2004**, *43*, 1115.
(44) (a) Hauser, J. J.; Waszczak, J. V. *Phys. Rev. B* **1984**, *30*, 5167. (b) Goff, R. J.; Williams, A. J.; Attfield, J. P. *Phys. Rev. B* **2004**, *70*, 014426. (c) Ortega-San Martin, L.; Chapman, J. P.; Lezama, L.; Sánchez Marcos, J.; Rodríguez-Fernández, J.; Arriortua, M. I.; Rojo, T. *Eur. J. Inorg. Chem.* **2006**, 1362.
(45) Bassani, F. *Handbook of Condensed Matter Physics*; Elsevier Ltd.: Amsterdam, The Netherlands, 2005; Vol. 5, p 312.
(46) Mydosh, J. A. *Spin Glasses: An Experimental Introduction*; Taylor & Francis: London, 1993.
(47) Moorjani, K.; Coey, J. M. D. In *Magnetic Glasses, Methods and Phenomena*; Wolsky, S. P., Czanderna, A. W., Eds.; Elsevier: Amsterdam, The Netherlands, 1984; Vol. *6*.
(48) Debye, P. *Ann. Phys.* **1912**, *344*, 789.
(49) Goodenough, J. B. *Magnetism and the Chemical Bond*; Interscience: New York, 1963.
(50) de Pedro, I.; Rojo, J. M.; Rodríguez Fernández, J.; Sanchez Marcos, J.; Fernández-Díaz, M. T.; Rojo., T. *J. Solid State Chem.* **2012**, *188*, 1.